Unveiling the mechanisms of motion of synchro-Shockley dislocations in Laves phases

Zhuocheng Xie, Dimitri Chauraud, Achraf Atila, Erik Bitzek, Sandra Korte-Kerzel, Julien Guénolé

Unveiling the mechanisms of motion of synchro-Shockley dislocations in Laves phases

Zhuocheng Xie [1], Dimitri Chauraud [2], Achraf Atila [2,3], Erik Bitzek [2,3], Sandra Korte-Kerzel [1], and Julien Guénolé [4,5,*]

[1] *Institute of Physical Metallurgy and Materials Physics, RWTH Aachen University, 52056 Aachen, Germany*

[2] *Max-Planck-Institut für Eisenforschung GmbH, Max-Planck-Str. 1, 40237 Düsseldorf, Germany*

[3] *Department of Materials Science and Engineering, Institute I: General Materials Properties, Friedrich-Alexander-Universität Erlangen-Nürnberg, 91058 Erlangen, Germany*

[4] *Université de Lorraine, CNRS, Arts et Métiers, LEM3, 57070 Metz, France*

[5] *Labex Damas, Université de Lorraine, 57070 Metz, France*

(Received 26 July 2022; accepted 4 April 2023; published 12 May 2023)

In Laves phases, synchroshear is the dominant basal slip mechanism. It is accomplished by the glide of synchro-Shockley dislocations. However, the atomic-scale mechanisms of motion of such zonal dislocations are still not well understood. In this paper, using atomistic simulations, two 30° synchro-Shockley dislocations with different Burgers vectors and core structures and energies are identified. We demonstrate that nucleation and propagation of kink pairs is the energetically favorable mechanism for the motion of the synchro-Shockley dislocation (partial I). Vacancy hopping and interstitial shuffling are identified as two key mechanisms related to kink propagation, and we investigated how vacancies and antisite defects assist kink nucleation and propagation, which is crucial for kink mobility. Additionally, we identified a mechanism of nonsequential atomic shuffling for the motion of the synchro-Shockley dislocation (partial II). These findings provide insights into the dependency on temperature and chemical composition of plastic deformation induced by zonal dislocations in Laves phases and the many related topologically close-packed phases.

DOI: 10.1103/PhysRevMaterials.7.053605

I. INTRODUCTION

Laves phases are topologically close-packed structures that form in many alloys and have a large impact on their mechanical properties due to the high strength compared with the matrix phases [1–3]. Laves-phase alloys often exhibit excellent mechanical properties at high temperatures; however, their extreme brittleness at ambient temperatures limits their applications as structural materials [3–5]. The understanding of the underlying deformation mechanisms of Laves phases is thus crucial for tailoring material properties of the composites.

Laves phases with the ideal chemical composition AB_2 have three common polytypes: Cubic $MgCu_2$(C15), hexagonal $MgZn_2$ (C14), and $MgNi_2$(C36). Laves crystals have a layered structure along the basal or {111} plane, which consists of quadruple atomic layers. The quadruple atomic layers in turn consist of a single-layer of B-type atoms forming a Kagomé net and a triple-layer with an A–B–A structure. The same layers also form part of the related structures as an intergrowth with other structural elements, such as $CaCu_5$ and Zr_4Al_3, the latter forming the μ phases [6,7].

Synchroshear, as a dominant mechanism for dislocation-mediated plasticity on the basal plane in Laves phases, was predicted in the 1960s [8]. It was later confirmed by experimental observations of synchro-Shockley dislocations and synchroshear-induced stacking faults in the C14 $HfCr_2$ Laves phase [9]. Recently, *ab initio* calculations [10] and atomistic simulations using semiempirical potentials [11] confirmed synchroshear as the energetically favorable mechanism compared with other crystallographic slip mechanisms for basal slip in Laves phases. Synchro-Shockley dislocations, a type of zonal dislocation [12,13], are formed by the cooperative motion of two coupled Shockley partial dislocations on the adjacent planes of a triple layer [14]. After the glide of a synchro-Shockley dislocation in a C14 (or C15) Laves phase, the alternate triple-layer transforms into a slab of C15 (or C14) structure, thus forming a stacking fault, i.e., synchroshear in Laves phases is always associated with the creation and extension of a stacking fault.

In Laves phases, point defects such as antisite atoms and vacancies widely exist in off-stoichiometric compositions and at high temperatures [3,15]. The presence of these point defects has significant effects on the deformation behavior, such as hardness [16–18] and phase transformation kinetics [19]. A progressive decrease in hardness at B-type-rich off-stoichiometric compositions was reported in nanoindentation experiments on $NbCo_2$ [16,18] and $NbFe_2$ [16,17] Laves phases. Single-phase $NbCr_2$ exhibits a more rapid synchroshear-induced phase transformation than its $TiCr_2$ and $TaCr_2$ counterparts, and the transformation is rendered sluggish by the addition of substitutional defects [19]. These experimental observations were attributed to the interactions between synchro-Shockley dislocations with constitutional and thermal point defects affecting the dislocation mobility [17,19].

Although existence and the geometry of slip by synchroshear is well established, the atomic-scale mechanisms of motion of synchro-Shockley dislocations on the basal plane in Laves phases are still not well understood. Kink propagation

*julien.guenole@univ-lorraine.fr

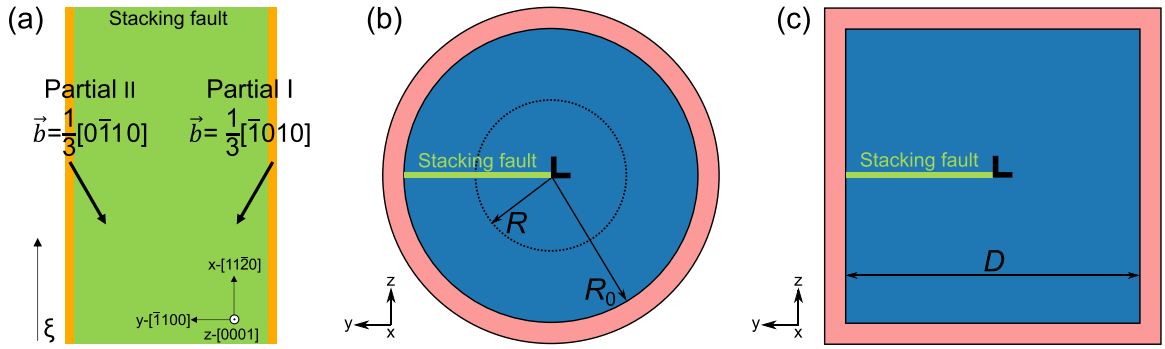

FIG. 1. (a) Schematic representation of the dissociated basal screw $\langle a \rangle$ dislocation in hexagonal Laves phases into two 30° synchro-Shockley dislocations: Partials I and II. (b) Cylindrical setup for the structural optimization of dislocation cores and the calculation of dislocation core energies. The radius of the cylindrical setup (R_0) is ∼1000 Å. (c) Slab setup for the nudged elastic band (NEB) calculation of minimum energy path (MEP) of dislocation motion. The dimensions of the slab (D) in nonperiodic directions are ∼300 Å. Periodic boundary conditions are applied along the dislocation line direction (ξ) in both setups. Semifixed outer layers where atoms are frozen in nonperiodic directions are marked in light red, and the thickness is >2 times the interatomic potential cutoff >14 Å. Please note that the shown setup corresponds to partial I; for partial II, the stacking fault is on the right of the dislocation.

and short-range diffusion were proposed as possible mechanisms of dislocation motion in Laves phases in the 1990s [14]; however, there has been no evidence from experiments or modeling. In addition, the effects of point defects on dislocation motion in Laves phases are yet to be explored.

In this paper, the core structures and energies of synchro-Shockley dislocations in C14 and C15 Laves phases were investigated using atomistic simulations. The mechanisms of motion of synchro-Shockley dislocations with and without point defects and corresponding activation energies were determined by identifying transition states on the potential energy surfaces. As the stacking fault has been confirmed as the dominant defect structure on the basal slip plane in Laves phases, instead of of the motion of perfect dislocations [9,14], the motion of synchro-Shockley dislocations was aligned to the direction of expansion of the stacking fault.

II. SIMULATION METHODS

The atomistic simulations presented in this paper were performed using the molecular dynamics software package LAMMPS [20]. The interatomic interactions were modeled by the modified embedded atom method (MEAM) potential by Kim *et al.* [21] for Mg-Ca, and the MEAM potential by Jang *et al.* [22] was used for the Al-Ca system. Both potentials reasonably describe the mechanical properties of C14 $CaMg_2$ and C15 $CaAl_2$ Laves phases as compared with experiments and *ab initio* calculations (see Table SI in the Supplemental Material [23]), e.g., the Kim potential shows a close match of the basal stacking fault energy of C14 $CaMg_2$ compared with the density functional theory (DFT) value. Additionally, both potentials successfully predicted the synchroshear as the energetically favorable mechanism for propagating dislocations within the basal and {111} planes in C14 $CaMg_2$ [11] and C15 $CaAl_2$ Laves phases, respectively.

The C14 $CaMg_2$ and C15 $CaAl_2$ Laves structures were constructed using Atomsk [24] with the lattice constant a_0 of the respective Laves phase at 0 K [21,22] and the following crystallographic orientations: For C14, $\mathbf{x} = [11\bar{2}0]$, $\mathbf{y} = [\bar{1}100]$, and $\mathbf{z} = [0001]$; for C15, $\mathbf{x} = [1\bar{1}0]$, $\mathbf{y} = [11\bar{2}]$, and $\mathbf{z} = [111]$.

To obtain the structures for the further study of synchro-Shockley partial dislocations, perfect screw dislocations with Burgers vectors $\mathbf{b}_{C14} = a_0^{C14}/3[\bar{1}\bar{1}20]$ and $\mathbf{b}_{C15} = a_0^{C15}/2[\bar{1}10]$ were introduced following the method detailed in Ref. [25]. After relaxation using the conjugate gradient with box relaxation and the FIRE [26,27] algorithm (force tolerance: 10^{-8} eV/Å), the inserted full screw dislocation dissociated into two widely separated 30° synchro-Shockley dislocations with Burgers vectors $\mathbf{b}_{C14} = a_0^{C14}/3[\bar{1}010]$ and $a_0^{C14}/3[0\bar{1}10]$ (for C15 $CaAl_2$, $\mathbf{b}_{C15} = a_0^{C15}/6[\bar{1}2\bar{1}]$ and $a_0^{C15}/6[\bar{2}11]$) bounded by stacking faults, see the sketch in Fig. 1(a). In the following, the partial dislocation on the right with the edge Burgers vector component along the $[\bar{1}100]$ (or $[11\bar{2}]$ for C15 $CaAl_2$) direction is termed partial I, and the partial dislocation on the left with the edge Burgers vector component along the $[1\bar{1}00]$ (or $[\bar{1}\bar{1}2]$ for C15 $CaAl_2$) direction is called partial II. To investigate partial I and II dislocations separately, the atomic displacement field corresponding to the partial Burgers vector was imposed to the upper half of the crystal ($>l_z/2$) from the end to the center of the simulation box. After relaxation with the abovementioned algorithms, partials I and II located at the center of the simulation box with a stacking fault bounded to the box end were obtained.

To calculate the core energies of the 30° synchro-Shockley dislocations, cylindrical samples were cut out from the initial simulation box (l_y, $l_z \approx 2000$ Å) with each of the 30° partial dislocations located in the center of the simulation setup, and the stacking fault bounded at the surface of the cylinder, as shown in Fig. 1(b). Atoms in the outermost layers of the setups with a thickness of 14 Å (2 times the interatomic potential cutoff) were fixed in y and z directions. The radius of the cylindrical setup is ∼1000 Å to reduce the effect of the boundary conditions. Periodic boundary conditions (PBCs) were applied in the x direction (the direction of the dislocation line). For C14 $CaMg_2$, $l_x \approx 18.4$ Å, containing 3 unit cells; for C15 $CaAl_2$, $l_x \approx 23.6$ Å, containing 2 unit cells. In both cases, l_x is >2 times larger than the interatomic potential cutoff.

After relaxation with the aforementioned boundary conditions, the core energies were calculated by measuring the total dislocation energy as a function of radius R and then extrapolating the far-field elastic energy back to the chosen cutoff radius ($r_c = b$):

$$E_{\text{tot}}(R) - N(R)E_0 = K\ln(R/r_c) + E_{\text{SF}}(R) + E_{\text{core}}|r_c, \quad (1)$$

where $E_{\text{tot}}(R)$ is the energy of the N atoms contained within a cylinder of radius R, E_0 is the atomic cohesive energy of the given composition, K is an elasticity coefficient containing anisotropic elastic constants [13] and the Burgers vector b, $E_{\text{SF}}(R)$ is the energy contribution of the stacking fault as a function of radius R, and $E_{\text{core}}|r_c$ is the core energy defined at the chosen cutoff radius $r_c = b$. Note that, as the stacking fault extends all the way to the edge of the simulation setup, $E_{\text{SF}}(R)$ is continuously increasing with R. Finally, the excess in strain energy E_{ESE} due to the elastic distortion of the lattice induced by the dislocation, normalized with the dislocation line length L, can be expressed from Eq. (2):

$$E_{\text{ESE}}(R) = \frac{E_{\text{tot}}(R) - N(R)E_0}{L}. \quad (2)$$

where E_{ESE} was calculated at 100 different R values from $1b$ to $250b$.

Climbing image nudged elastic band (NEB) [28,29] calculations were performed on initial (before dislocation motion) and final (after dislocation motion) atomistic configurations to find saddle points and minimum energy paths (MEPs) of dislocation motion. The initial configurations were built with the 30° partial dislocations located in the center of the slab setups, as illustrated in Fig. 1(c). By altering the width of the displacement field for the inserted partial Burgers vector applied on the upper half of the crystal (see Ref. [25] for details), the final configuration contains the same partial dislocation sitting at the next Peierls valley adjacent to the initial one, corresponding to dislocation motion and expansion of the stacking fault by one Burgers vector. Atoms in the outermost layers of the setups with a thickness of 14 Å were fixed in y and z directions. The dimensions of the slab in y and z directions l_y and $l_z \approx 300$ Å. Slab setups with different dislocation line lengths (in PBC) from 3× to 30× unit cells (l_x from 18.4 to 184.2 Å for C14 $CaMg_2$) were simulated.

The spring constants for parallel and perpendicular nudging forces are both 1.0 eV/Å^2 [30]. QUICKMIN [31] was used as the damped dynamics minimizer to minimize the energies across all replicas with the force tolerance of 0.01 eV/Å. Different numbers of intermediate replicas from 48 to 144 were simulated, and all intermediate replicas were initially equally spaced along the reaction coordinate (RC). The first (RC 0) and last (RC 1) RCs were determined as the configurations located at the local energy minima along the MEP close to the initial and final configurations, respectively, and were fully relaxed before the NEB calculations.

An atomic structural analysis method for Laves phases, Laves phase crystal analysis (LaCA) [32], was used to analyze the dislocation and stacking fault structures in C14 and C15 Laves phases. LaCA can be seen as an advanced common neighbor analysis method [33], which combines identification of Frank-Kasper clusters with centrosymmetry to unambiguously classified atomic arrangements in Laves crystals [32]. For visualization and analysis of atomistic simulations, OVITO [34] was used.

III. RESULTS

A. Dislocation core energies and structures

Core structures of 30° synchro-Shockley dislocations were analyzed, and the corresponding core energies were calculated according to Eq. (1). Two types of 30° synchro-Shockley dislocations with Burgers vectors of $\frac{1}{3}[\bar{1}010]$ (partial I) and $\frac{1}{3}[0\bar{1}10]$ (partial II) were obtained after the energy minimization of the perfect screw dislocations. Both core structures of partials I [Fig. 2(b)] and II [Fig. 2(c)] were observed in Laves crystal structures experimentally [9,35,36]. Dislocation core energies of partials I and II were calculated by extrapolating the far-field elastic energy back to the chosen cutoff radius b, see Fig. 2(a). The excess in strain energy E_{ESE} was plotted against the logarithm of the ratio of R/b in Fig. 2(a). The deviation of potential energy within the radius $R < 2b$ is significant, as shown in Figs. 2(b) and 2(c) (and Figs. S1(b) and S1(c) in the Supplemental Material [23]). In contrast, the atoms belonging to the stacking faults show less energy deviation due to the low stacking fault energies of the Laves phases ($\gamma_{\text{SF}}^{\text{CaMg}_2} = 14$ mJ/m^2 and $\gamma_{\text{SF}}^{\text{CaAl}_2} = 52$ mJ/m^2). The slope of the total energy E_{tot} vs $\ln(R/b)$ is close to linear for radii R significantly larger than the core region except when R approaches the semifixed boundary, which agrees with elasticity theory. A linear model was fitted to the data of E_{ESE} vs $\ln R/b$ from $5b$ to $100b$. An elasticity coefficient $[K/(b^2/4\pi) = 27.8$ GPa] was obtained, which is within a deviation of <2% from the theoretical K value $[K_{\text{elast}}^{30^\circ}/(b^2/4\pi) = 27.3$ GPa] calculated considering basal plane isotropy in hexagonal crystals [13] and using the elastic constants of the interatomic potential (see Table SI in the Supplemental Material [23]):

$$K_{\text{elast}}^{\theta} = K_{\text{elast}}^{0^\circ}\cos^2\theta + K_{\text{elast}}^{90^\circ}\sin^2\theta, \quad (3)$$

$$K_{\text{elast}}^{0^\circ} = \frac{b^2}{4\pi}(C_{44}C_{66})^{1/2}, \quad (4)$$

$$K_{\text{elast}}^{90^\circ} = \frac{b^2}{4\pi}(\bar{C}_{11} + C_{13})\left[\frac{C_{44}(\bar{C}_{11} - C_{13})}{C_{33}(\bar{C}_{11} + C_{13} + 2C_{44})}\right]^{1/2}, \quad (5)$$

$$\bar{C}_{11} = (C_{11}C_{33})^{1/2}. \quad (6)$$

For the $\theta = 30^\circ$ synchro-Shockley dislocation in the simulated C14 $CaMg_2$, the elasticity coefficient of the screw component $K_{\text{elast}}^{0^\circ}/(b^2/4\pi)$ is 25.6 GPa, and the value of the edge component $k_{\text{elast}}^{90^\circ}/(b^2/4\pi)$ is 32.6 GPa.

The core energies of partial I and II dislocations at the chosen cutoff radius $r_c = b$ are 0.16 and 0.28 eV/Å, respectively. The core energy of partial II is 75% higher than partial I, which indicates that partial I is more energetically favorable than partial II in the simulated C14 $CaMg_2$ phase. Similar results were also obtained in the simulated C15 $CaAl_2$ phase, as shown in Fig. S1(a) in the Supplemental Material [23].

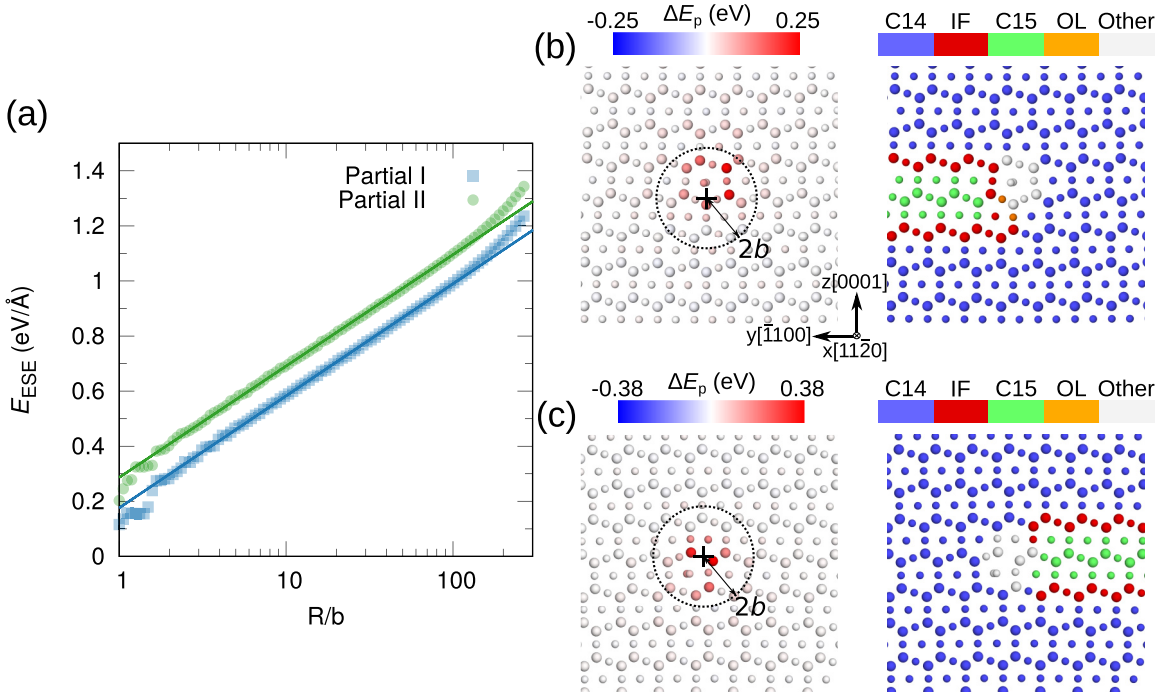

FIG. 2. (a) Excess in elastic strain energy E_{ESE} for 30° synchro-Shockley partials I ($\mathbf{b} = \frac{1}{3}[\bar{1}010]$) and II ($\mathbf{b} = \frac{1}{3}[0\bar{1}10]$) dislocations in C14 $CaMg_2$. The core energy is obtained by extrapolating the far-field elastic energy back to the chosen cutoff radius $r_c = b$ ($R/b = 1$, solid lines). Dislocation core structures of 30° synchro-Shockley (b) partial I and (c) partial II dislocations. Left: Colored by deviation of potential energy to bulk (ΔE_p). Right: Colored by Laves phase crystal analysis (LaCA). Large and small atoms are Ca and Mg atoms, respectively.

B. Mechanisms of dislocation motion

The mechanisms of synchro-Shockley dislocation motion were investigated by exploring the transition states between two dislocation structures at adjacent Peierls valleys along the MEP using the NEB method. Overall, we investigated the mechanisms of motion for both partials I and II and also the effect of point defects on the motion of partial I, where point defects were found to form as part of the dislocation motion.

1. Motion of partial I

Partial I in C14 $CaMg_2$ exhibits a transition mechanism of dislocation motion via kink-pair nucleation and kink propagation, as shown in Fig. 3(a). The bow-out of a kink-pair occurs around the RC 0.13 with a height of the edge component of the partial Burgers vector, which corresponds to the motion of the dislocation from one Peierls valley to the next. Then the two kinks propagate in opposite directions and finally merge with each other due to the PBC along the dislocation line direction. The motion of partial I is along the $[1\bar{1}00]$ direction. The energy profile of the transition processes of kink-pair nucleation and kink propagation is shown in Fig. 3(b). Transition state peaks and intermediates with similar shapes and values in the energy profile appear repeatedly, which indicates similar events are repeatedly activated along the MEP. The transition mechanism of partial I motion can be divided into several stages: Nucleation (Nucl.), I, II, III, and merging of the kink pair (Merg.). The detailed mechanism of each stage is illustrated in Fig. 3(c) via the atomic displacement relative to the initial configuration (RC 0). To better visualize the individual events between the transition states, only atoms in the triple layer where the dislocation glides are shown since most atomic movements occurred within the triple layer. The Ca atoms in different layers within the triple layer are colored with different shades of red.

In the nucleation stage (from RC 0 to 0.13), a Ca atom (colored dark red) shuffles from top to bottom (the direction along x-$[11\bar{2}0]$ is defined as up for ease of reference here) into the lattice and creates a vacancy (marked by an orange circle) and an interstitial in the triple layer. Meanwhile, the nearby atoms downward from the Ca atom along the dislocation line shuffle together. The nucleation of the kink pair can be treated as the formation of two kinks. The formation of the upper and lower kinks are associated with the formation of vacancy and interstitial defects, respectively. The energy barrier of the kink-pair nucleation is 2.33 eV, which is the highest activation energy among all individual events along the MEP of the motion of partial I. Therefore, the kink-pair nucleation process is the rate-limiting step on the RC diagram. The energy barriers of overall and individual events along the MEP of dislocation motion in this paper are summarized in Table I. In stage I (from RC 0.13 to 0.20), the Mg atom above the Ca vacancy shuffles to the vacancy and creates another Mg vacancy. This process has an activation energy of ∼1.03 eV. Following stage I, stage II (from RC 0.20 to 0.25) corresponds to the shuffling of a Ca atom (colored dark red) to the Mg vacancy and the creation of a Ca vacancy. The activation energy of this event is ∼0.29 eV, which is the lowest activation energy of the individual events along the MEP. The combination of stages I and II corresponds to

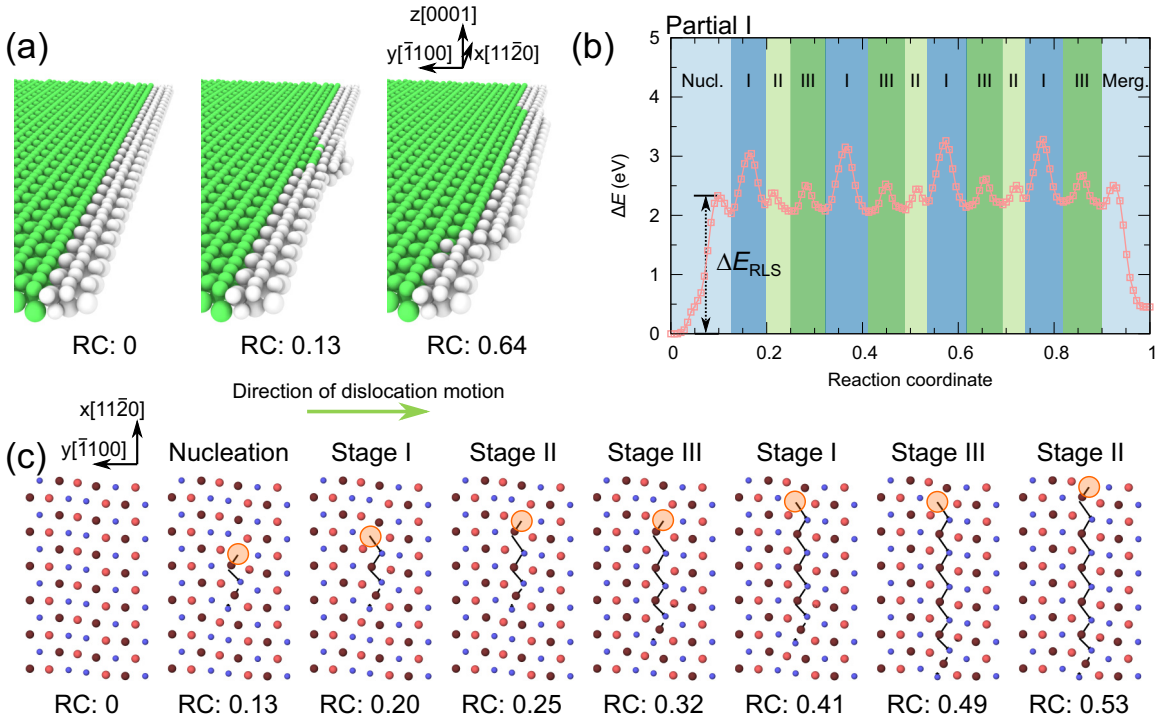

FIG. 3. Transition mechanism of 30° synchro-Shockley partial I dislocation motion along the [1$\bar{1}$00] direction (i.e., negative y direction, see the coordinate system) via kink propagation in C14 $CaMg_2$ ($l_x = 6.1$ nm, $l_y = l_z = 30$ nm). (a) Atomic configurations of kink nucleation and propagation. Only atoms belong to the stacking fault (C15, colored in green) and dislocation core (others, colored in white) according to Laves phase crystal analysis (LaCA) are shown here. (b) Excess energy vs reaction coordinate (RC) is calculated using nudged elastic band (NEB). The energy profile is separated into different stages based on individual activation events. The activation energy of the rate-limiting step ΔE_{RLS} is marked in the plot. (c) Mechanisms of kink nucleation and propagation. Only atoms in the triple layer where the dislocation glided are shown here. Large and small atoms are Ca and Mg atoms, respectively. Dark and light red atoms indicate Ca atoms in different layers of the triple layer. Black arrows indicate displacement vectors (RC 0 configuration as the reference). Orange circles indicate the locations of vacancies. Green arrow indicates the direction of dislocation motion.

the propagation of the upper kink from bottom to top via repeated formation and occupation of vacancies. Stage III corresponds to the propagation of the lower kink from top to bottom via an interstitiallike mechanism with an energy barrier of ∼0.46 eV. The Mg and Ca atoms (colored dark red) below the lower kink shuffle simultaneously and create an interstitial defect at the dislocation core region. In the following events of kink propagation, stages I, III, and II repeatedly occur until the kinks merge with an activation energy of 0.35 eV. The final state exhibits higher energy than the initial one because of the expansion of the stacking fault after the motion of the partial dislocation. The largest energy barrier to the motion of partial I is 3.28 eV. In general, for partial I, the mechanism of dislocation motion is kink-pair formation and propagation in which the kinks propagate via two mechanisms, namely, vacancy hopping and interstitial shuffling, depending on the character of the kinks.

Similar mechanisms were identified for partial I dislocations with a longer dislocation length $l_x = 18.4$ nm (Fig. S2 in the Supplemental Material [23]) and different num-

TABLE I. Activation energies of overall and individual events of the motion of synchro-Shockley dislocations in C14 $CaMg_2$ ($l_x = 6.1$ nm, $l_y = l_z = 30$ nm). $V_X\perp$: vacancy at X site at dislocation; $(XY)\perp$: Antisite defect X at Y site at dislocation.

		Activation energy (eV)				
Sample	Overall	Nucleation	Stage I	Stage II	Stage III	Merge
Partial I	3.28	2.33	1.03	0.29	0.46	0.35
Partial I ($V_{Mg}\perp$)	1.53	—	1.01	0.24	—	—
Partial I ($V_{Ca}\perp$)	1.40	—	0.99	0.26	—	—
Partial I [Mg(Ca)⊥]	2.59	1.75	1.03	0.21	—	0.39
Partial I [Ca(Mg)⊥]	3.15	2.29	1.08	—	0.46	0.32
Sample	Overall	Nonsequential shuffling		Shear straining	Rearrangement	
Partial II	1.79	0.31		1.10	0.11	

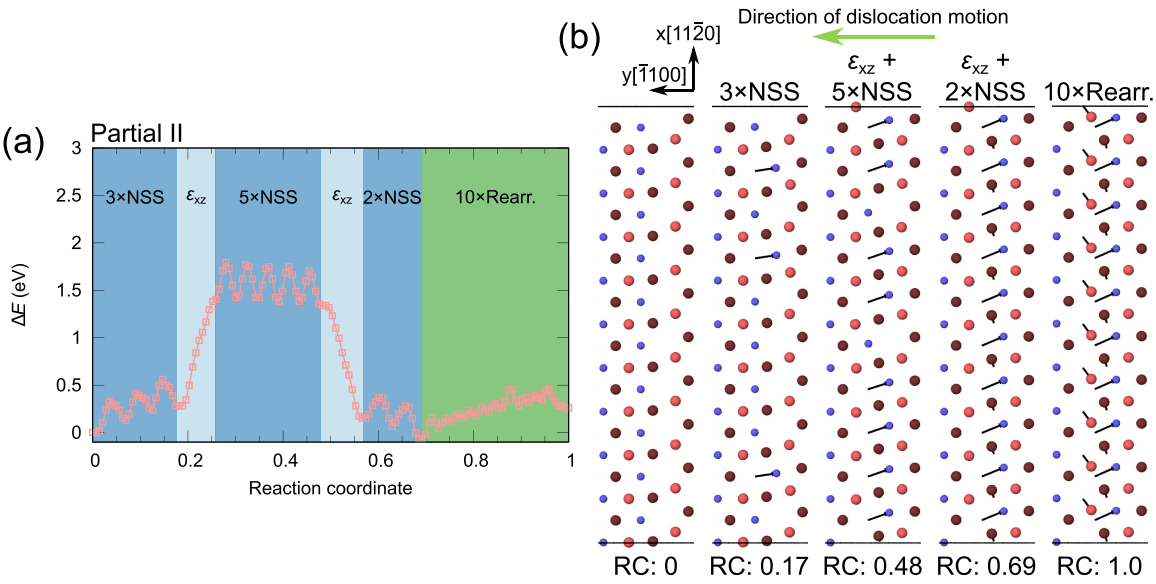

FIG. 4. Motion of 30° synchro-Shockley partial II dislocation along the [$\bar{1}$100] direction via diffusionlike mechanism in C14 $CaMg_2$ ($l_x = 6.1$ nm, $l_y = l_z = 30$ nm). (a) Excess energy vs reaction coordinate is calculated using nudged elastic band (NEB). (b) Diffusionlike mechanism mixed of nonsequential shuffling (NSS), shear straining (ϵ_{xz}) and short-range rearrangement (Rearr.). Only atoms in the triple layer where the dislocation glided are shown here. Large and small atoms are Ca and Mg atoms, respectively. Dark and light red atoms indicate Ca atoms in different layers of the triple layer. Black arrows indicate displacement vectors (RC 0 configuration as the reference). Green arrow indicates the direction of dislocation motion.

bers of intermediate replicas (Fig. S3 in the Supplemental Material [23]). In contrast, the two-dimensional (2D) setup with $l_x = 1.8$ nm is too small to resolve the complex reactions of kink-pair nucleation and propagation. Instead, the synchronous movement of the Ca (colored dark red) and Mg atoms with one saddle point along the MEP is obtained (see Fig. S4 in the Supplemental Material [23]). Although the stacking fault energy of the simulated C15 $CaAl_2$ is significantly higher than for C14 $CaMg_2$ (see Table SI in the Supplemental Material [23]), similar kink-pair nucleation and propagation mechanisms were identified (see Fig. S5 in the Supplemental Material [23]).

2. *Motion of partial II*

The partial II dislocation shows a different mechanism of dislocation motion than partial I. Instead of sequential atomic shuffling during kink propagation of partial I, partial II in C14 $CaMg_2$ exhibits a nonsequential atomic shuffling during its motion. In addition, the two coupled Shockley partial dislocations of partial II move separately. To investigate the mechanism of motion of the leading partial dislocation (extension of the stacking fault), the motion of partial II is along the y ([$\bar{1}$100]) direction.

The energy profile and detailed mechanism of partial II dislocation motion are shown in Fig. 4. Like the energy profile of partial I, the reaction path of the motion of partial II can be divided into individual events and separated stages, see Fig. 4(a). Between RC 0 and 0.17, three nonadjacent Mg atoms (in the Mg sublattice along the dislocation line) shuffle to the adjacent free volume sites separately, as shown in Fig. 4(b). Three similar peaks with an average energy barrier of 0.31 eV are obtained for these nonsequential shufflings (NSSs). After that, a shear straining (ϵ_{xz}) along the x ([11$\bar{2}$0]) direction takes place with an activation energy of 1.1 eV, followed by five NSSs of Mg atoms (from RC 0.17 to 0.48). The shear straining step has the largest energy difference among all individual events along the MEP of partial II motion. After RC 0.48, an energy drop with the same magnitude as the increase of the energy due to the shear straining occurs because of the release of stored elastic energy. After the NSS of two Mg atoms, the motion of the first of the two coupled Shockley partial dislocations is completed. The motion of the second Shockley partial is carried out by the shuffling of the Ca atoms (colored light red) with an average activation energy of 0.11 eV, which corresponds to an atomic rearrangement (Rearr.) of the dislocation core. The overall energy barrier of partial II dislocation motion is 1.79 eV.

The 2D setup with $l_x = 1.8$ nm exhibits a similar mechanism that also consists of three stages including NSS, shear straining, and atomic rearrangement (see Fig. S6 in the Supplemental Material [23]). The activation energy of the shear straining of the 2D setup is 0.33 eV which is proportional to the dislocation length (l_x) with the same value per unit length (0.018 eV/Å) as the three-dimensional (3D) setup ($l_x = 6.1$ nm), which indicates the shear straining process is not a localized activation event.

3. *Effect of point defects on the motion of partial I*

As the motion of partial I is associated with the formation and motion of point defects along the dislocation line, we further investigated the effect of the presence of preexisting point defects on the partial dislocation motion. Taking the ordered structure of Laves phases into account, we considered vacancies and antisite defects on both the Mg and Ca

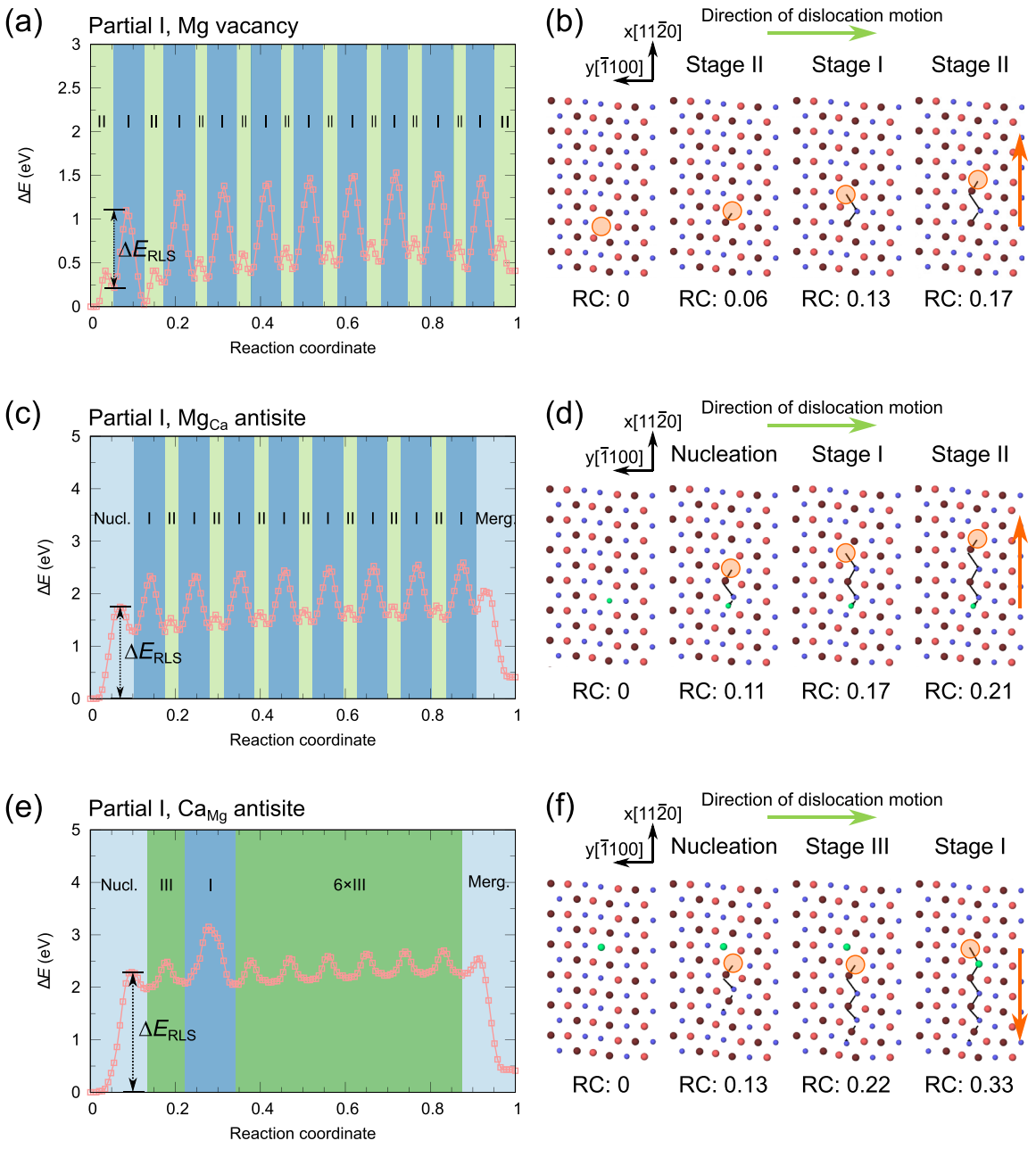

FIG. 5. Kink propagation of 30° synchro-Shockley partial I dislocation with point defects in C14 $CaMg_2$ ($l_x = 6.1$ nm, $l_y = l_z = 30$ nm): (a) and (b) Mg vacancy, (c) and (d) Mg_{Ca}, and (e) and (f) Ca_{Mg} antisites. (a), (c), and (e) Excess energy vs reaction coordinate (RC) is calculated using nudged elastic band (NEB). (b) and (d) Vacancy hopping is the governed mechanism of kink propagation of the dislocations with vacancies and Mg_{Ca} antisite. (f) Interstitiallike mechanism governs the kink propagation of the dislocation with Ca_{Mg} antisite. Only atoms in the triple layer where the dislocation glided are shown here. Large and small atoms are Ca and Mg atoms, respectively. Dark and light red atoms indicate Ca atoms in different layers of the triple layer. Green atoms indicate antisite defects. Black arrows indicate displacement vectors (RC 0 configuration as the reference). Orange circles indicate the locations of vacancies. Orange and green arrows mark the directions of kink propagation and dislocation motion, respectively.

sublattices in the dislocation core region within the triple layer. The formation energies of these point defects in the simulated Laves phases at the dislocation core region and the bulk counterparts are listed in Table SII in the Supplemental Material [23].

The observed mechanisms are presented in Fig. 5 (and Fig. S7 in the Supplemental Material [23]). The energy profile and atomistic mechanism of motion of partial I with one Mg vacancy are shown in Figs. 5(a) and 5(b). To construct atomistic samples with a Mg vacancy, the same Mg atom within the triple layer along the dislocation line was removed in both initial and final configurations. The energy profile of motion of partial I with the Mg vacancy can be separated into two individual activation events. In contrast to the mechanism of a pristine partial I dislocation (see Fig. 3), no kink nucleation stage is presented as the kink nucleus was introduced by the

preexisting Mg vacancy. Instead, the shuffling of a Ca atom (colored dark red) to the preexisting Mg vacancy triggers the propagation of the kink (from RC 0 to 0.06). This event is like stage II as described in the mechanism of pristine partial I dislocation motion with a comparable activation energy of ∼0.24 eV, therefore also named stage II here. From RC 0.06 to 0.13, the Mg atom above the Ca atom along the dislocation line shuffles to the Ca vacancy created after the first stage II. The activation energy of this event is ∼1.01 eV, which is the highest among all transition events and again close to stage I as described in the mechanism of pristine partial I dislocation motion and corresponding to a similar atomic shuffling. Thus, this event is also named stage I. In the following reaction path, stages II and I repeatedly occur, and the kink only propagates from bottom to top, which is dominated by the vacancy-hopping mechanism. Similarly, in the partial I dislocation motion with a Ca vacancy, stages I (with an average activation energy of 0.99 eV) and II (with average activation energy of 0.26 eV) also repeatedly occur, see Fig. S7 in the Supplemental Material [23]. The vacancy-hopping mechanism dominates the propagation of the kink from bottom to top. The values of ΔE_{RLS} of the partial I dislocation motion with the Mg and Ca vacancies are 1.01 and 1.09 eV, respectively. These values are much lower than the rate-limiting energy barrier of the pristine counterpart.

NEB calculations were also performed on the partial I dislocations with preexisting antisite defects at the dislocation core region. For this, a Ca or Mg atom was replaced by a Mg or Ca atom in both initial and final atomistic configurations. Figures 5(c), 5(d) and 5(e), 5(f) show the energy profiles and mechanisms of dislocation motion with $\mathrm{Mg_{Ca}}$ and $\mathrm{Ca_{Mg}}$ antisite defects, respectively, where the subscript indicates the original elemental species at this lattice position. In the case of the $\mathrm{Mg_{Ca}}$ antisite, a kink-pair nucleation event occurs at the beginning of the reaction path (from RC 0 to 0.11), which corresponds to the shufflings of the $\mathrm{Mg_{Ca}}$ antisite atom (colored in green) together with a Ca atom (colored dark red) and a Mg atom above the antisite defect, as shown in Fig. 5(d). A Ca vacancy is generated at the upper kink, and a Mg interstitial defect of the antisite atom is formed at the lower kink. The energy barrier of the kink-pair nucleation in the partial I with the $\mathrm{Mg_{Ca}}$ antisite is 1.75 eV, which is the rate limiting step, and the value is lower than the pristine counterpart. In the following reaction path, the upper kink propagates upward via the vacancy-hopping mechanism, and the lower kink is pinned at the interstitial defect. Stages I and II of the antisite decorated partial I have similar activation energies (1.03 and 0.21 eV for stages I and II, respectively) and similar atomic shuffling mechanisms to the pristine partial I dislocation. The two stages take place repeatedly in the motion of the partial I dislocation with the $\mathrm{Mg_{Ca}}$ antisite.

Different from the vacancy-hopping-dominated mechanism in partial I with preexisting vacancies and a $\mathrm{Mg_{Ca}}$ antisite defect, a partial I with a $\mathrm{Ca_{Mg}}$ antisite shows an interstitial-shuffling mechanism of dislocation motion [see Figs. 5(e) and 5(f)]. The kink-pair nucleation is associated with the shufflings of Ca atoms (colored dark red) and the Mg atom below the $\mathrm{Ca_{Mg}}$ antisite (colored green) and the generation of a Ca vacancy. The energy barrier of kink-pair nucleation is 2.29 eV, which is the rate-limiting step and close to the value of the pristine counterpart. In the rest of the reaction path, the $\mathrm{Ca_{Mg}}$ antisite atom shuffles to the Ca vacancy with an activation energy of 1.08 eV, close to the energy barrier of stage I. Then the upper kink is pinned at the vacancy. The presence of five Ca atoms surrounding the vacancy leads to a high packing density and therefore a small free volume. As a result, the vacancy-hopping mechanism is no longer energetically favorable. Instead, the lower kink propagates downward via the interstitiallike mechanism with an average activation energy of 0.46 eV, like stage III as described for the pristine counterpart.

IV. DISCUSSION

A. Direction dependence of plasticity

Two 30° synchro-Shockley dislocations with edge components of Burgers vectors in opposite directions and different core structures were identified, as shown in Figs. 1(a) and 2(b), 2(c). These partial dislocations, named partials I and II here, possess different core energies, which indicates these two dislocations also have different critical stresses for nucleation. Depending on which partial dislocation is more geometrically (higher Schmid factor) and/or energetically (lower activation energy) favorable, nucleation-controlled plasticity could therefore exhibit directional dependencies.

Additionally, the two synchro-Shockley dislocations are expected to exhibit different critical resolved shear stresses for motion due to different mechanisms of motion and corresponding activation energies. Specifically, partials I and II exhibit different self-pinning characters during the dislocation motion.

The motion of a synchro-Shockley dislocation, also known as a zonal dislocation, can be regarded as the cooperative motion of two coupled Shockley partial dislocations on adjacent planes of the triple layer. The motion of partial I dislocations is dominated by the kink-pair propagation and requires consecutive motion of the two coupled Shockley partial dislocations, i.e., in the vacancy-hopping-dominant dislocation motion, as given in Table I. The energy barrier at 0 K for the motion of one of the coupled Shockley dislocations (corresponding to stage II with an energy barrier $\Delta E_{\mathrm{stage\ II}} \approx 0.25$ eV) is much lower than the other one (corresponding to stage I with an energy barrier $\Delta E_{\mathrm{stage\ I}} \approx 1.03$ eV). Thus, the thermally activated kink propagation requires the activation of two consecutive thermally activated mechanisms. If one of these is unsuccessful, especially the one with higher activation energy, then the total synchro-Shockley dislocation becomes temporarily immobile, which is referred to as the self-pinning nature of synchro-Shockley dislocations in Laves phases [37,38].

For partial II, the shear straining process has a higher energy barrier than the two thermally activated events (NSS and short-range rearrangement). Thermal activation could only control the motion of partial II if the applied shear strain/stress reaches a certain level to overcome the corresponding energy barrier. In addition, the motions of the two coupled Shockley partial dislocations of partial II occur separately, namely, the motion of one of the Shockley partial dislocations (corresponding to the series of NSS processes)

takes place first and is then followed by the other Shockley partial dislocation (which moves by the series of short-range rearrangement processes). Unlike the self-pinning character of partial I, the thermally activated motion of partial II does not require consecutive thermal activation of events with different energy barriers.

These observations could be investigated experimentally using micro/nanopillar compression. The nucleation-controlled plasticity may be expected to manifest in micro/nanopillar compression tests on defect-free single-crystal Laves phases oriented to maximize resolved shear stresses on either partial I or II dislocation. In contrast, variations in the lattice friction and thermal activation of the partial dislocation motion may be accessible by compression of similarly oriented single-crystalline pillars but with a preexisting dislocation density at different rates and temperatures. However, the controlled preparation of such samples is challenging, and whether the expected effects will be possible to resolve given the experimental uncertainties and the need to suppress fracture remains to be explored.

B. Point-defect-assisted dislocation motion

Point defects, including vacancies and antisite atoms, very commonly exist in Laves phases and have significant effects on mechanical properties [3,15]. For the Mg-Al-Ca alloying system, first-principles calculations on stoichiometric C14 $CaMg_2$ [39] and C15 $CaAl_2$ [40] suggest the predominance of constitutional antisite and vacancy defects, respectively.

The dislocation core region is more energetically favorable for the formation of point defects than the perfect and unstrained Laves crystal lattice, as shown in Table SII in the Supplemental Material [23]. Therefore, the constitutional point defects are likely to locate at preexisting dislocations and thus affect the mechanisms of dislocation motion and corresponding activation energy. In this paper, the key mechanism of vacancy-assisted kink propagation, namely, vacancy hopping, is demonstrated by NEB calculations. Furthermore, the presence of a vacancy at the dislocation core region dramatically reduces the energy barriers of kink-pair nucleation. In the simulated C14 $CaMg_2$, the presence of V_{Mg} and V_{Ca} lower the activation energies of the rate limiting step ΔE_{RLS} of dislocation motion by 57 and 58%, respectively.

Antisite defects have also been proposed to affect the hardness of Laves phases with off-stoichiometric compositions [15–18], and progressive softening behavior with deviations from stoichiometric Laves phases has indeed been observed in previous experiments [16–18]. In this paper, a possible origin of this behavior is unveiled by considering the influence of segregated antisite defects at the dislocation core on the mechanism and activation energy of kink-pair nucleation and propagation. In the simulated C14 $CaMg_2$ phase, the effect of antisite defects on the rate-limiting activation barrier of dislocation motion is a reduction ranging from 2 to 25% depending on the antisite type. The effect of Mg_{Ca} antisite defects is much more pronounced than Ca_{Mg} antisite defects. The reason for this is that a small Mg atom on a large Ca atom site generates excess free volume, making it easier for the lattice to adapt to the formation of vacancy and interstitial during kink nucleation, thus facilitating the vacancy-hopping mechanism of kink propagation. This finding agrees well with the experimental results that the softening was observed in off-stoichiometric compounds that were rich in the smaller B atoms [16,17].

The thermal fluctuation can not only lower the critical stress of dislocation motion but also speed up the atomic diffusion which results in the formation of thermal vacancies [15,40]. At finite temperatures below the temperatures in which diffusion enables diffusion-based mechanisms of motion, a significant number of vacancies will favor vacancy-hopping mechanisms and thus have a prominent effect on the mechanisms of dislocation motion.

How the different activation barriers for the migration of the two kinks affect the overall mobility and resulting shapes of the partial I dislocation for different stresses and temperatures will depend on multiple factors, including the pinning distance of the dislocations, the types of obstacles for dislocation motion, the mean free path for dislocation motion, the rates of nucleation and annihilation of kinks, and the concentration and mobility of point defects. All these factors are outside the scope of this paper but could be addressed by, e.g., kinetic Monte Carlo (kMC) simulations, like in Refs. [41–43]. The identified activation events and correlated activation energy barriers determined in this paper could serve as input parameters for developing a kMC model of dislocation motion in Laves phases. The kMC model could allow investigations of dislocation dynamics comprising various kinds of events with atomistically informed activation rates.

C. Generalizability of the mechanisms

The outcomes of this paper, namely, the mechanisms of direction-dependent and point-defect-assisted motion of synchro-Shockley dislocations in C14 $CaMg_2$ and C15 $CaAl_2$ Laves phases, could be generalized to other Laves phases and crystal structures containing Laves crystal building blocks, such as μ phases.

In this paper, two distinct core structures and core energies of partial I and II dislocations were identified in C14 $CaMg_2$ and C15 $CaAl_2$ Laves phases (see Figs. 2 and S1 in the Supplemental Material [23]). Dislocations often have different equivalent and nonequivalent core structures resulting from the symmetry of the crystal lattice [44]. In Laves crystal structures, the atomic arrangement within the triple layer is different at two ends of the synchroshear-induced stacking fault along the $\langle a \rangle$ or $\langle 110 \rangle$ direction (see Fig. S8 in the Supplemental Material [23]). The surrounding atomic distributions of the smaller B atoms at the end of the stacking fault (with a Burgers vector of $\frac{1}{3}$ $[\bar{1}010]$ or $\frac{1}{6}$ $[\bar{1}2\bar{1}]$ corresponding to the extension of the stacking fault relative to the matrix) are noncentrosymmetric (see Figs. S8(e) and S8(f) in the Supplemental Material [23]). In contrast, the smaller B atoms at the opposite end of the stacking fault (with the Burgers vector of $\frac{1}{3}$ $[0\bar{1}10]$ or $\frac{1}{6}$ $[\bar{2}11]$) exhibit a centrosymmetric atomic environment within the triple layer. Therefore, partial I and II dislocations bounding the synchroshear-induced stacking fault with 30° Burgers vectors symmetric with respect to the dislocation line direction ($\langle a \rangle$ or $\langle 110 \rangle$ direction) have different core structures and energies. Accordingly, different nucleation criteria and

mobilities of partial I and II dislocations are expected to generally exist on the deformation-mechanism maps of Laves crystal building blocks. Similar observations were reported in diamondlike [45,46] and perovskite structures [47], where the dislocations with identical/symmetric Burgers vectors have different core structures at low and high temperatures, thus exhibiting temperature-dependent mobilities.

The kink-pair mechanism is a dislocation glide mode across Peierls valleys as a consequence of high lattice friction [44]. In previous atomistic studies, the nucleation and propagation of kink pairs were found to control the glide of screw dislocations in body-centered cubic iron [48,49], silicon [50,51], and perovskite crystals [52,53], where the activation volume of the kink-pair nucleation is only a few b^3. Laves phases are notoriously brittle at low temperature due to the difficulty in moving dislocations under external shear stress [3,4]; therefore, the kink-pair mechanism is believed to govern the motion of synchro-Shockley dislocations which serve as the carrier of plasticity at high temperature. The nature of kink-pair-controlled dislocation motion in the simulated Laves phases correlates well with the experimental estimations on the activation volume of C14 $CaMg_2$ ($\Omega = 13b^3$, based on the experimental data obtained from micropillar compression tests [54,55] and the calculation details described in Ref. [23]) and other Laves phases [37,38,56,57]. Furthermore, we believe the effects of vacancy and antisite defects on the kink-pair mechanism of dislocation motion are not limited to specific Laves compounds. It was speculated that the presence of a vacancy or antisite defect at the site of a kink would facilitate the motion of synchro-Shockley dislocations from the geometry and packing density of Laves crystal structure [17,19].

V. CONCLUSIONS

In this paper, we investigated the mechanisms of motion of 30° synchro-Shockley dislocations in C14 $CaMg_2$ and C15 $CaAl_2$ Laves phases using atomistic simulations. The MEP of dislocation motion and corresponding activation energies were determined using the NEB method.

Our aim was to reveal the mechanisms of motion of synchro-Shockley partial dislocations in Laves phases and to begin to understand the physical origins of changing mechanical properties of Laves phases containing point defects as a result of temperature and stoichiometry changes. From this paper, we conclude that

(1) Two types of 30° synchro-Shockley dislocations with different Burgers vectors (referred to as partials I and II) were identified in the simulated C14 $CaMg_2$ and C15 $CaAl_2$ Laves phases and observed experimentally in other Laves or structurally similar phases. Partial I exhibits a lower core energy than partial II; it is therefore expected to have a lower critical nucleation stress.

(2) Partial I dislocation propagates via kink-pair nucleation and propagation. Kink-pair nucleation on partial I dislocations is accomplished by creating a vacancy and interstitial pair. The kink pair then propagates via vacancy-hopping and interstitial-shuffling mechanisms in two directions along the dislocation line separately.

(3) The motion of partial II dislocation in C14 $CaMg_2$ consists of three stages including nonsequential atomic shuffling, shear straining, and atomic rearrangement. The shear straining process exhibits the largest energy difference among these individual stages and is not a localized activation event. In contrast, the nonsequential atomic shuffling and atomic rearrangement processes are highly localized events.

(4) The presence of point defects at the dislocation core significantly lowers the energy barrier for the motion of the partial I dislocation in C14 $CaMg_2$. In the cases of vacancies and the B_A antisite defect, the activation energy of kink-pair nucleation is dramatically reduced, and the propagation of one of the kinks is dominated by the vacancy-hopping mechanism.

ACKNOWLEDGMENTS

The authors acknowledge financial support by the Deutsche Forschungsgemeinschaft (DFG) through Projects No. A02, No. A05, and No. C02 of the SFB1394 Structural and Chemical Atomic Complexity—From Defect Phase Diagrams to Material Properties, Project ID 409476157. This project has received funding from the European Research Council under the European Union's Horizon 2020 research and innovation programme (Grant Agreement No. 852096 FunBlocks). E.B. gratefully acknowledges support from the Deutsche Forschungsgemeinschaft through Project No. C3 of the Collaborative Research Centre SFB/TR 103. Simulations were performed with computing resources granted by RWTH Aachen University under Project No. rwth0591, by the Erlangen Regional Computing Center (RRZE) and by the EXPLOR center of the Université de Lorraine and by the GENCI-TGCC (Grant No. 2021-A0100911390 and 2022-A0120911390). We acknowledge Dr. Ali Tehranchi (Max-Planck-Institut für Eisenforschung GmbH) for providing the DFT data. Z.X. would like to thank Dr.-Ing. Wei Luo (RWTH Aachen University) for fruitful discussions.

[1] A. K. Sinha, Topologically close-packed structures of transition metal alloys, Prog. Mater. Sci. **15**, 81 (1972).

[2] P. Paufler, Early work on Laves phases in East Germany, Intermetallics **19**, 599 (2011).

[3] F. Stein and A. Leineweber, Laves phases: A review of their functional and structural applications and an improved fundamental understanding of stability and properties, J. Mater. Sci. **56**, 5321 (2021).

[4] J. Livingston, Laves-phase superalloys? Phys. Stat. Sol. (a) **131**, 415 (1992).

[5] T. M. Pollock, Weight loss with magnesium alloys, Science **328**, 986 (2010).

[6] E. Parthé, B. Chabot, M. Penzo, K. Cenzuel, and R. Gladyshevskii, *Gmelin Handbook of Inorganic and Organometallic Chemistry: TYPIX. Standardized Data and Crystal Chemical Characterization of Inorganic Structure Types* (Springer, Berlin, 1993), Vol. 1 pp. 147, 169.

[7] S. Schröders, S. Sandlöbes, B. Berkels, and S. Korte-Kerzel, On the structure of defects in the Fe_7Mo_6 μ-phase, Acta Mater. **167**, 257 (2019).

[8] U. Krämer and G. Schulze, Gittergeometrische Betrachtung der plastischen Verformung von Lavesphasen, Krist. Techn. **3**, 417 (1968).

[9] M. F. Chisholm, S. Kumar, and P. Hazzledine, Dislocations in complex materials, Science **307**, 701 (2005).

[10] O. Vedmedenko, F. Rösch, and C. Elsässer, First-principles density functional theory study of phase transformations in $NbCr_2$ and $TaCr_2$, Acta Mater. **56**, 4984 (2008).

[11] J. Guénolé, F.-Z. Mouhib, L. Huber, B. Grabowski, and S. Korte-Kerzel, Basal slip in Laves phases: The synchroshear dislocation, Scr. Mater. **166**, 134 (2019).

[12] M. Kronberg, Plastic deformation of single crystals of sapphire: Basal slip and twinning, Acta Metall. **5**, 507 (1957).

[13] P. M. Anderson, J. P. Hirth, and J. Lothe, *Theory of Dislocations* (Cambridge University Press, Cambridge, 2017).

[14] P. Hazzledine, K. Kumar, D. Miracle, and A. Jackson, Synchroshear of Laves phases, MRS Online Proc. Lib. **288**, 591 (1992).

[15] J. Zhu, L. Pike, C. Liu, and P. Liaw, Point defects in binary Laves phase alloys, Acta Mater. **47**, 2003 (1999).

[16] S. Voß, F. Stein, M. Palm, D. Grüner, G. Kreiner, G. Frommeyer, and D. Raabe, Composition dependence of the hardness of Laves phases in the Fe-Nb and Co-Nb systems, MRS Online Proc. Lib. **1128**, 805 (2008).

[17] N. Takata, H. Ghassemi-Armaki, M. Takeyama, and S. Kumar, Nanoindentation study on solid solution softening of Fe-rich Fe_2Nb Laves phase by Ni in Fe–Nb–Ni ternary alloys, Intermetallics **70**, 7 (2016).

[18] W. Luo, C. Kirchlechner, J. Li, G. Dehm, and F. Stein, Composition dependence of hardness and elastic modulus of the cubic and hexagonal $NbCo_2$ Laves phase polytypes studied by nanoindentation, J. Mater. Res. **35**, 185 (2020).

[19] K. Kumar and P. Hazzledine, Polytypic transformations in Laves phases, Intermetallics **12**, 763 (2004).

[20] A. P. Thompson, H. M. Aktulga, R. Berger, D. S. Bolintineanu, W. M. Brown, P. S. Crozier, P. J. in 't Veld, A. Kohlmeyer, S. G. Moore, T. D. Nguyen *et al.*, LAMMPS—A flexible simulation tool for particle-based materials modeling at the atomic, meso, and continuum scales, Comput. Phys. Commun. **271**, 108171 (2022).

[21] K.-H. Kim, J. B. Jeon, and B.-J. Lee, Modified embedded-atom method interatomic potentials for Mg–X (X = Y, Sn, Ca) binary systems, Calphad **48**, 27 (2015).

[22] H.-S. Jang, D. Seol, and B.-J. Lee, Modified embedded-atom method interatomic potentials for Mg–Al–Ca and Mg–Al–Zn ternary systems, J. Magnesium Alloys **9**, 317 (2021).

[23] See Supplemental Material at http://link.aps.org/supplemental/10.1103/PhysRevMaterials.7.053605, containing Tables SI and SII, Figs. S1– S8, and details on the experimental estimation of activation volume. Supplemental Material also contains Refs. [54,55,58–64].

[24] P. Hirel, Atomsk: A tool for manipulating and converting atomic data files, Comput. Phys. Commun. **197**, 212 (2015).

[25] A. Vaid, D. Wei, E. Bitzek, S. Nasiri, and M. Zaiser, Pinning of extended dislocations in atomically disordered crystals, Acta Mater. **236**, 118095 (2022).

[26] E. Bitzek, P. Koskinen, F. Gähler, M. Moseler, and P. Gumbsch, Structural Relaxation Made Simple, Phys. Rev. Lett. **97**, 170201 (2006).

[27] J. Guénolé, W. G. Nöhring, A. Vaid, F. Houllé, Z. Xie, A. Prakash, and E. Bitzek, Assessment and optimization of the fast inertial relaxation engine (fire) for energy minimization in atomistic simulations and its implementation in LAMMPS, Comput. Mater. Sci. **175**, 109584 (2020).

[28] G. Henkelman, B. P. Uberuaga, and H. Jónsson, A climbing image nudged elastic band method for finding saddle points and minimum energy paths, J. Chem. Phys. **113**, 9901 (2000).

[29] G. Henkelman and H. Jónsson, Improved tangent estimate in the nudged elastic band method for finding minimum energy paths and saddle points, J. Chem. Phys. **113**, 9978 (2000).

[30] E. Maras, O. Trushin, A. Stukowski, T. Ala-Nissila, and H. Jónsson, Global transition path search for dislocation formation in Ge on Si(001), Comput. Phys. Commun. **205**, 13 (2016).

[31] D. Sheppard, R. Terrell, and G. Henkelman, Optimization methods for finding minimum energy paths, J. Chem. Phys. **128**, 134106 (2008).

[32] Z. Xie, D. Chauraud, E. Bitzek, S. Korte-Kerzel, and J. Guénolé, Laves phase crystal analysis (LaCA): Atomistic identification of lattice defects in C14 and C15 topologically close-packed phases, J. Mater. Res. **36**, 2010 (2021).

[33] J. D. Honeycutt and H. C. Andersen, Molecular dynamics study of melting and freezing of small Lennard-Jones clusters, J. Phys. Chem. **91**, 4950 (1987).

[34] A. Stukowski, Visualization and analysis of atomistic simulation data with OVITO—The Open Visualization Tool, Modell. Simul. Mater. Sci. Eng. **18**, 015012 (2010).

[35] W. Zhang, R. Yu, K. Du, Z. Cheng, J. Zhu, and H. Ye, Undulating Slip in Laves Phase and Implications for Deformation in Brittle Materials, Phys. Rev. Lett. **106**, 165505 (2011).

[36] Y. Cheng, G. Wang, J. Liu, and L. He, Atomic configurations of planar defects in μ phase in Ni-based superalloys, Scr. Mater. **193**, 27 (2021).

[37] A. Kazantzis, M. Aindow, I. Jones, G. Triantafyllidis, and J. T. M. De Hosson, The mechanical properties and the deformation microstructures of the C15 Laves phase Cr_2Nb at high temperatures, Acta Mater. **55**, 1873 (2007).

[38] A. Kazantzis, M. Aindow, G. Triantafyllidis, and J. T. M. De Hosson, On the self-pinning character of synchro-Shockley dislocations in a Laves phase during strain rate cyclical compressions, Scr. Mater. **59**, 788 (2008).

[39] L. Shao, T.-T. Shi, J. Zheng, X.-Z. Pan, and B.-Y. Tang, The native point defects in C14 Mg_2Ca Laves phase: A first-principles study, Intermetallics **65**, 29 (2015).

[40] X. Tian, J.-N. Wang, Y.-P. Wang, X.-F. Shi, and B.-Y. Tang, First-principles investigation of point defect and atomic diffusion in Al_2Ca, J. Phys. Chem. Solids **103**, 6 (2017).

[41] W. Cai, V. V. Bulatov, S. Yip, and A. S. Argon, Kinetic Monte Carlo modeling of dislocation motion in BCC metals, Mater. Sci. Eng. A **309-310**, 270 (2001).

[42] A. Stukowski, D. Cereceda, T. D. Swinburne, and J. Marian, Thermally-activated non-Schmid glide of screw dislocations in W using atomistically-informed kinetic Monte Carlo simulations, Int. J. Plast. **65**, 108 (2015).

[43] S. Shinzato, M. Wakeda, and S. Ogata, An atomistically informed kinetic Monte Carlo model for predicting solid solution

strengthening of body-centered cubic alloys, Int. J. Plast. **122**, 319 (2019).

[44] D. Caillard and J.-L. Martin, *Thermally Activated Mechanisms in Crystal Plasticity* (Elsevier, Oxford, 2003).

[45] H. Koizumi, Y. Kamimura, and T. Suzuki, Core structure of a screw dislocation in a diamond-like structure, Philos. Mag. A **80**, 609 (2000).

[46] A. T. Blumenau, M. I. Heggie, C. J. Fall, R. Jones, and T. Frauenheim, Dislocations in diamond: Core structures and energies, Phys. Rev. B **65**, 205205 (2002).

[47] P. Gumbsch, S. Taeri-Baghbadrani, D. Brunner, W. Sigle, and M. Rühle, Plasticity and an Inverse Brittle-to-Ductile Transition in Strontium Titanate, Phys. Rev. Lett. **87**, 085505 (2001).

[48] M. Wen and A. Ngan, Atomistic simulation of kink-pairs of screw dislocations in body-centred cubic iron, Acta Mater. **48**, 4255 (2000).

[49] S. Narayanan, D. L. McDowell, and T. Zhu, Crystal plasticity model for BCC iron atomistically informed by kinetics of correlated kinkpair nucleation on screw dislocation, J. Mech. Phys. Solids **65**, 54 (2014).

[50] L. Pizzagalli, A. Pedersen, A. Arnaldsson, H. Jónsson, and P. Beauchamp, Theoretical study of kinks on screw dislocation in silicon, Phys. Rev. B **77**, 064106 (2008).

[51] L. Pizzagalli, Atomistic modeling of the dissociation of a screw dislocation in silicon, J. Mater. Sci. **51**, 2869 (2016).

[52] A. M. Goryaeva, P. Carrez, and P. Cordier, Low viscosity and high attenuation in $MgSiO_3$ post-perovskite inferred from atomic-scale calculations, Sci. Rep. **6**, 34771 (2016).

[53] A. Kraych, P. Carrez, P. Hirel, E. Clouet, and P. Cordier, Peierls potential and kink-pair mechanism in high-pressure $MgSiO_3$ perovskite: An atomic scale study, Phys. Rev. B **93**, 014103 (2016).

[54] M. Freund, D. Andre, C. Zehnder, H. Rempel, D. Gerber, M. Zubair, S. Sandlöbes-Haut, J. S.-L. Gibson, and S. Korte-Kerzel, Plastic deformation of the $CaMg_2$ C14-Laves phase from 50–250°C, Materialia **20**, 101237 (2021).

[55] C. Zehnder, K. Czerwinski, K. D. Molodov, S. Sandlöbes-Haut, J. S.-L. Gibson, and S. Korte-Kerzel, Plastic deformation of single crystalline C14 Mg_2Ca laves phase at room temperature, Mater. Sci. Eng., A **759**, 754 (2019).

[56] Y. Ohba and N. Sakuma, High temperature-room temperature deformation behavior of $MgCu_2$ Laves phase intermetallic compound, Acta Metall. **37**, 2377 (1989).

[57] H. Saka, T. Hayakawa, M. Nakamura, H. Mizutani, and E. Nakamura, Plasticity of single crystals of Fe_2 (Dy, Tb) Laves phase at high temperatures, Philos. Mag. A **68**, 871 (1993).

[58] H. Nowotny, Die Kristallstrukturen von Zn_9Th, Cd_2Ca und $(Ag, Mg)_2Ca$, Int. J. Mater. Res. **37**, 31 (1946).

[59] R. Arróyave and Z.-K. Liu, Intermetallics in the Mg-Ca-Sn ternary system: Structural, vibrational, and thermodynamic properties from first principles, Phys. Rev. B **74**, 174118 (2006).

[60] R. Schiltz Jr and J. Smith, Elastic constants of some MAl_2 single crystals, J. Appl. Phys. **45**, 4681 (1974).

[61] W.-Y. Yu, N. Wang, X.-B. Xiao, B.-Y. Tang, L.-M. Peng, and W.-J. Ding, First-principles investigation of the binary AB_2 type Laves phase in Mg-Al-Ca alloy: Electronic structure and elastic properties, Solid State Sci. **11**, 1400 (2009).

[62] A. Sumer and J. Smith, Elastic constants of single-crystal $CaMg_2$, J. Appl. Phys. **33**, 2283 (1962).

[63] S. Ganeshan, S. Shang, H. Zhang, Y. Wang, M. Mantina, and Z. Liu, Elastic constants of binary Mg compounds from first-principles calculations, Intermetallics **17**, 313 (2009).

[64] A. Tehranchi, T. Hickel, and J. Neugebauer, Max-Planck-Institut für Eisenforschung, Düsseldorf, Germany (2022) (private communication).